

Scalable and Sustainable Cathode Regeneration from Blended Spent Batteries into Stable Lithium-Rich Manganese-Based Cathodes

Haiyan Qin, Xia Sun, Tingzhou Yang,* Pengrong Zhang, Haochen Dong, Ning Liu,* Yongguang Zhang,* and Zhongwei Chen*

As a vital urban mineral resource, the efficient recycling of spent lithium-ion batteries (LIBs) is crucial for mitigating resource scarcity and environmental pollution, especially for obtaining high-value cathode materials through various regeneration methods. Herein, a large-scale recyclable and sustainable direct cathode regeneration strategy is explored to obtain stable lithium-rich manganese-based cathode materials via a customized continuous stirred tank reactor, enabling the transition to next-generation high-energy-density LIBs via battery recycling. A high recycling efficiency between 97.38% and 99.93% is achieved for high-value transition metal elements, and the regenerated next-generation higher-specific capacity

cathode materials with higher lattice oxygen and lower oxygen vacancy demonstrate better structural stability and improved electrochemical performance than corresponding commercial materials. Life cycle and technoeconomic analysis are used to highlight the cathode regeneration method, which exhibits significant advantages across all 18 midpoint and 3 endpoint environmental impact categories, with a 44.22% cost reduction compared to commercial materials. This commercialization strategy holds significant promise for advancing closed-loop battery recycling and minimizing environmental pollution in LIB production, offering a new perspective for sustainable battery recycling.

1. Introduction

As the world becomes increasingly reliant on convenience and power provided by lithium-ion batteries (LIBs), their raw material market will occupy a core position in future energy markets like oil, which plays a key role in ensuring national energy security.^[1–3] Global reserves of lithium (Li), cobalt (Co), and nickel (Ni) metals are unevenly distributed and scarce, where their mining and refining are labor and energy intensive and concomitant environmental pollution becomes increasingly serious.^[4,5] Compared with the random distribution of various mineral resources, the high-value metal resources in spent LIBs are more concentrated and have higher purity.^[6–8] As the most economically valuable type of further urban mining, the LIB recycling economy is

essential for the global raw material supply, which will be a critical secondary source.^[9] It is estimated that more than 11 million tons of spent LIB packs will be discarded between 2017 and 2030. However, only 16.4% of spent LIBs are recycled. Therefore, the recycling of spent batteries is imminent.^[10]

Up to now, there are three main recycling technologies for spent LIBs, which are combined in a different manner: hydrometallurgy,^[11–15] pyrometallurgy,^[16–19] and direct recycling processes.^[20–23] Most of the collected spent LIBs are recycled by a highly energetic process based on pyrometallurgy over 1200 °C, followed by complicated hydrometallurgy using strong mineral acids, where some elements, including Li and manganese (Mn), are inevitably lost or obtained metal salts are of very low purity.^[3,24] Fei et al.^[19] proposed a pyrometallurgical method that achieved a Li leaching rate of 99.39%; however, its high energy consumption and the emission of harmful gases raise significant environmental and operational concerns. Sun et al.^[25] regenerated $\text{LiNi}_{0.6}\text{Co}_{0.2}\text{Mn}_{0.2}\text{O}_2$ cathode material by combining pyrometallurgical and hydrometallurgical techniques using sulfuric acid with the leaching efficiency of 94.47%, 99.36%, 99.28%, and 99.56% for Li, Ni, Co, and Mn, respectively. The waste acid and byproducts generated during leaching processes posed considerable risks to both operators and the environment. Ma et al.^[20] proposed a strategy combining spent $\text{LiNi}_{0.5}\text{Co}_{0.2}\text{Mn}_{0.3}\text{O}_2$ with LiMn_2O_4 (LMO), where partial cobalt and nickel were preferentially removed to regenerate low-cobalt-doped $\text{LiNi}_{0.5}\text{Mn}_{1.5}\text{O}_4$ -type cathode materials. These regenerated materials exhibited significantly improved conductivity and bond strength, demonstrating exceptional cycling stability under both high-rate (10 °C and 20 °C) and high-temperature (60 °C) conditions. In contrast, our team, led by Yang et al.,^[26] has pioneered an innovative direct recycling method based on a

H. Qin, X. Sun, P. Zhang, H. Dong, N. Liu, Y. Zhang

School of Materials Science and Engineering

Hebei University of Technology

Tianjin 300130, China

E-mail: ningliu1985@hebut.edu.cn

ygzheng@dicp.ac.cn

T. Yang, Y. Zhang, Z. Chen

State Key Laboratory of Catalysis

Dalian Institute of Chemical Physics

Chinese Academy of Sciences

Dalian 116023, China

E-mail: tzyang@dicp.ac.cn

zwchen@dicp.ac.cn

T. Yang

School of Chemistry and Chemical Engineering

Nantong University

Nantong 226019, China



Supporting information for this article is available on the WWW under https://doi.org/10.1002/batt.202500316

leaching-coprecipitation process, where the regenerated cathode materials were comparable to commercial materials with a leaching rate over 99.8%. However, it is mainly used to recover Ni-rich cathode materials with limited energy density.

The escalating global demand for batteries has rendered enhanced energy density an essential imperative. Compared with Ni-rich cathode materials, Li-rich Mn-based ($\text{Li}_{1.2}\text{Mn}_{0.54}\text{Ni}_{0.13}\text{Co}_{0.13}\text{O}_2$, LRM) cathode materials have been regarded as one of the most promising candidates for next-generation high-energy-density LIBs due to their prominent specific capacity and low toxicity.^[27–29] The LRM, characterized by its high manganese content and balanced nickel-cobalt ratio, can be efficiently synthesized by using $\text{LiNi}_{1/3}\text{Co}_{1/3}\text{Mn}_{1/3}\text{O}_2$ (NCM111, NCM) as the base material and supplementing with LMO to boost manganese levels. This approach enables the optimal recycling of spent NCM111 and LMO to produce regenerated lithium-rich manganese(R-LRM) cathode materials while dramatically reducing the need for additional material inputs.^[30,31] Advancing next-generation battery materials represents a crucial pathway toward a sustainable energy transition, underscoring the imperative for simultaneous breakthroughs in battery recycling innovations to establish a closed-loop material ecosystem. This approach aligns with the core principles of green chemistry by minimizing environmental impact, reducing reliance on finite natural resources, and lowering the raw material costs associated with battery production, thereby fostering the sustainable development of battery technologies.

Herein, we propose a simple and scalable spent LIB recycling route via a set of customized Continuous Stirred Tank Reactor (CSTR) systems, which enables stable LRM that is better than commercial powders. More than 97.38% of high-value transition metal (TM) elements are recycled from black mass obtained from the blended spent LIBs based on LMO and NCM cathodes. The mixed black mass powder extraction strategy streamlines the leaching process, and the adoption of an acetic acid-based system significantly minimizes the environmental and occupational hazards associated with wastewater. The calcination process employing the dual-salt melting method endowed R-LRM with reduced oxygen vacancies and enhanced lattice oxygen content, demonstrating exceptional stability without structural collapse while improving cycling performance over 500 cycles. In addition, life cycle and techno-economic analyses suggest that our regenerated cathode manufacturing cost is 44.22% lower than that of corresponding commercial materials and has smaller resource scarcity, human health, and ecosystem quality impacts.

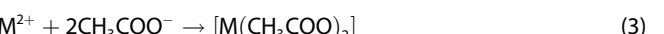
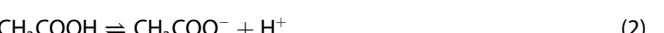
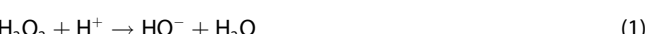
2. Results and Discussion

2.1. Regeneration of Recycled Cathodes

The black material was sourced from Wuhan GEM Co., Ltd., primarily consisting of NCM111 and LMO (Table S1). An improved cathode regeneration process based on hydrometallurgy is proposed for large-scale commercialized spent battery recycling based on two CSTRs connected by a self-developed acid-resistant filtration system in series, where one of them is used to

extract high-value TM elements from recycled black mass obtained from the blended spent LIBs, and the other 50 L CSTR is used to obtain new cathode material precursor through a co-precipitation regeneration process (Figure 1a and Figure S1).

In the first CSTR, only high-value elements, including Li, Mn, Co, and Ni, are extracted into the leachate, and unwanted impurities such as aluminum (Al), copper (Cu), and carbon (C) materials are removed. Conventional leaching processes usually use inorganic acids as the leaching agent, where some impurities such as Al and Cu can be inevitably dissolved into the leachate. These impurities from the current collectors and shells are difficult to separate from the leachate. If they participate in the coprecipitation reaction, the performance of the regenerated cathode material will be further deteriorated. However, acetic acid exhibits distinct behavior compared to other acids, where the relevant reactions involving transition metals are outlined below:



In oxygenated environments, aluminum forms a dense protective alumina layer, while copper develops passivating layers such as cuprous oxide or basic copper salts under mildly acidic and oxygen-rich conditions, both exhibiting strong resistance to acetic acid corrosion. Furthermore, aluminum acetate complexes hinder the sustained dissolution of metals due to poor solubility. Cu^+ ions are thermodynamically unstable in aqueous solution and tend to undergo disproportionation, which leads to the formation of Cu^{2+} and metallic Cu, which strongly catalyze the decomposition of hydrogen peroxide and peracetic acid. This catalytic activity results in the rapid depletion of oxidizing species near the metal-solution interface, thereby limiting the continued oxidative dissolution of copper.^[32,33] As shown in Figure S2, Cu dissolved in sulfuric acid solution has a concentration of 2000.00 ppm, and its content reaches up to 1010.00 ppm in nitric acid. Al dissolved in sulfuric acid solution has a concentration of 17.53 ppm, increasing to 1611.00 ppm in nitric acid. We use acetic acid as the leaching agent, which selectively extracts the high-value elements we need under low-oxygen conditions. 0.90 and 0.72 ppm of Al and Cu can be detected after a 5 h leaching process at 70 °C.

The extraction rates of LMO- and NCM-based black mass at different temperatures are investigated in Figure 1b, which delivers increasing extraction rates from 6.43 and 27.24 g L⁻¹ at 25 °C to 27.67 and 50.45 g L⁻¹ at 90 °C, respectively, further indicating that the extraction capability of TM elements is highly dependent on the reaction temperature. For LMO, the Jahn-Teller effect during the long-term cycles can accelerate the dissolution of Mn. Due to the presence of Ni species in the divalent state, the solubility of NCM is higher than that of LMO. The temperature-dependent extraction capability was also confirmed by the photographs of leachate under different reaction temperatures. The color variation of LMO leachate indicates different Mn extraction efficiencies at different temperatures, and a light pink color can be observed above 50 °C (Figure 1c). For NCM, the color changes

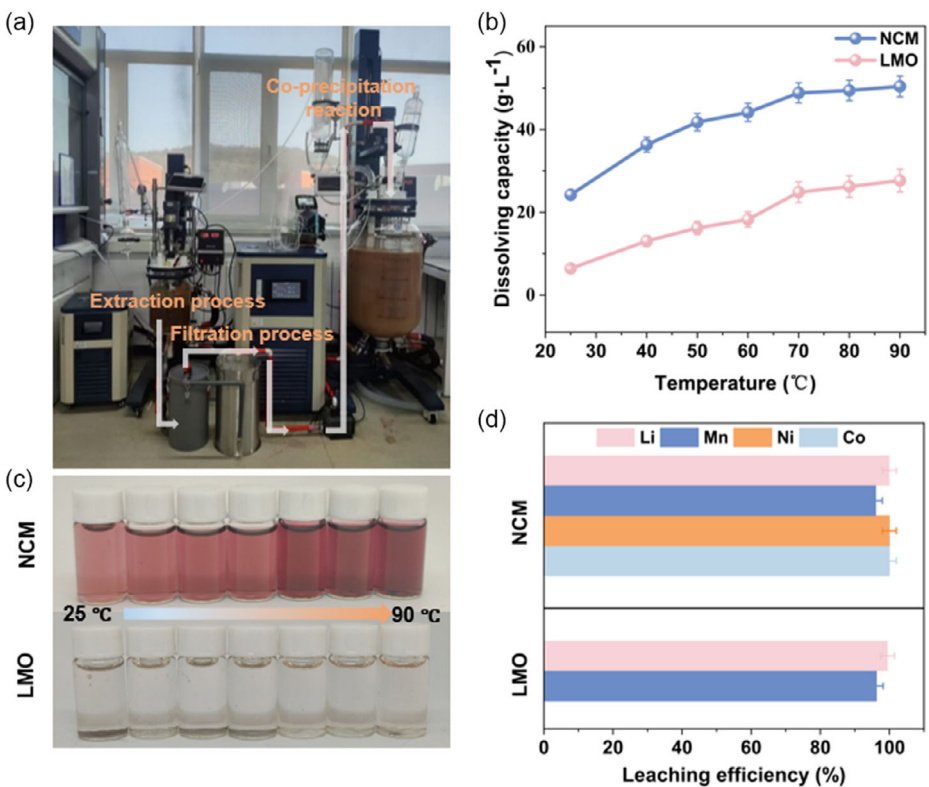


Figure 1. a) Self-designed continuous agitation reactor with acid-resistant filtration system for cathode regeneration. b) Effect of different temperatures on the extraction capacities of various spent cathodes. c) Photograph of the color change under different temperatures. d) Leaching efficiencies of each element from spent cathode powders under 70 °C.

from purple-red to dark purple as the temperature increases due to the increase in dissolved amount.^[24]

Although higher extraction capabilities are desirable, an appropriate extraction capacity matched with the subsequent co-precipitation process will yield the best gains in terms of energy consumption and low cost. Therefore, the most suitable reaction temperature was selected as 70 °C. The corresponding leaching efficiencies of each element for LMO and NCM with continuous stirring at 70 °C for 1 h are shown in Figure 1d. For LMO, more than 100.00% of Li and 96.26% of Mn were leached. Due to the similar ionic radii of Li⁺ and Ni²⁺, Li/Ni mixed arrangement is caused, which further promotes the collapse of the NCM structure, resulting in faster leaching kinetics with high leaching efficiencies of 100.00%, 100.00%, 100.00%, and 96.03% for Li, Ni, Co, and Mn, respectively. Moreover, X-ray diffraction (XRD) patterns were used to confirm that all high-value elements had been extracted in the leachate, where XRD curves of LMO- and NCM-based black mass showed their corresponding lattice structures (Figure S3). After the leaching process, the XRD curve of the impurities obtained by filtration indicates that the corresponding lattice structure has disappeared, and such high efficiency is very beneficial for large-scale recycling operations (Figure S4).

2.2. Characterization of Regenerated Cathodes

Subsequently, the filtered leachate was transferred to the reaction tank of the 50 L CSTR system. In the leachate, the highly oxidized

TM elements are reduced to divalent ions. The molar ratios between Mn, Co, and Ni are adjusted to 0.54: 0.13: 0.13 by adding extra LMO- and NCM-based leachate, without the need to add large amounts of TM acetate salts, further reducing the regenerated cathode manufacturing cost. A simple co-precipitation method is completed by adding NaHCO₃ in the reaction tank to obtain the carbonate precursor of Mn_{0.675}Co_{0.1625}Ni_{0.1625}CO₃. Ammonia is simultaneously added as a chelating agent to form a metal–ammonia complex with the TM substance in the reaction tank to prevent the precipitation of each phase during the co-precipitation process. When filtering out precursors, the solution became transparent, and all high-value metals were recovered through the spherical precursor with a high recycling efficiency of 99.93% (Mn), 99.61% (Co), and 97.38% (Ni) (Figure S5). The residual lithium ions are extracted by adding excess sodium carbonate at relatively high temperatures (Figure S6). The dual-salt melting method is employed during the calcination process, where the low melting temperature induced by the dual salts facilitates more uniform element diffusion (Figure S7). After replenishing Li ions, the R-LRM with a dense spherical structure is obtained, where the molar ratios between Li, Mn, Ni, and Co are further confirmed by inductively coupled plasma-optical emission spectrometer (ICP-OES, Table S2). As shown in Figure 2b, the input and output for regenerating 50 L of R-LRM are listed; 2.36 kg of recycled LMO and 2.18 kg of recycled NCM111 were used, resulting in 5.67 kg of precursor after the reaction, which produced 5.40 kg of R-LRM after high-temperature lithiation process.

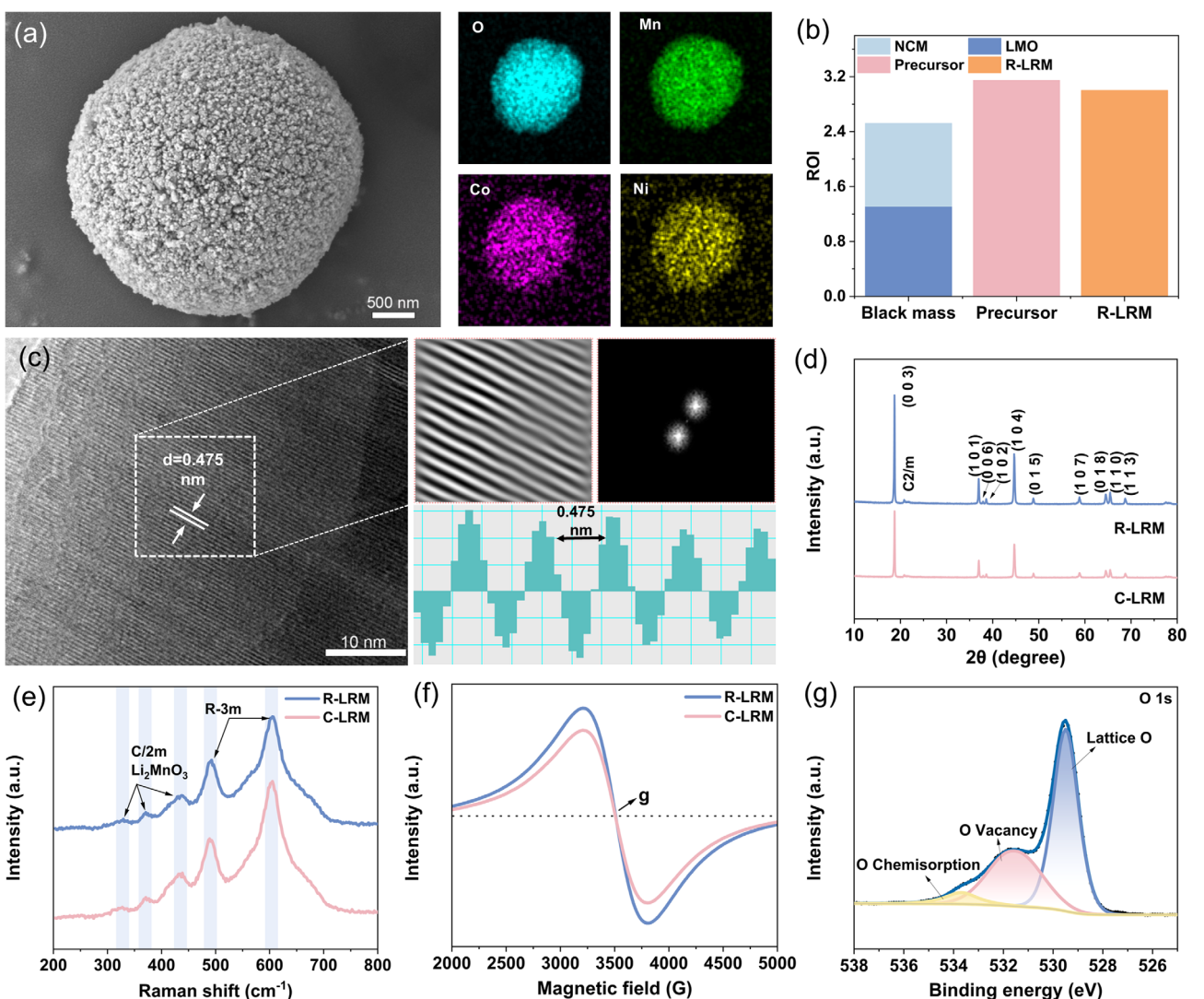


Figure 2. a) SEM image and EDS mapping images for R-LRM. b) Yield of black mass, precursor, and LRM in a single regeneration process. c) TEM image of R-LRM. d) XRD patterns of R-LRM and C-LRM. e) Raman spectra of R-LRM and C-LRM. f) EPR spectra of R-LRM and C-LRM. g) O 1s XPS spectrum of R-LRM.

The morphological features of regenerated materials were researched by scanning electron microscope (SEM) images, where the obtained precursor exhibits a dense spherical structure after the co-precipitation processes using recycled black mass (Figure S8). Followed by the double-salt fusion method during calcination, R-LRM still maintains the spherical structure with a diameter of 3.61 μm (Figure 2a). Corresponding energy dispersive spectroscopy (EDS) mapping images demonstrate a uniform distribution of Ni, Co, Mn, and O elements across the surface of R-LRM, indicating no elemental segregation. From the high-resolution transmission electron microscopy (HRTEM) image and the corresponding fast Fourier transform pattern of R-LRM, a well-crystallized (003) plane can be observed (Figure 2c). The interplanar spacing was determined to be 0.475 nm, which is significantly higher than that of commercial state-of-the-art LRM (C-LRM) cathode (0.472 nm), further confirming that our co-precipitation strategy with the double-salt fusion method during calcination using recycled materials results in a well-defined layered structure of cathode materials with wider distances, which accelerates the diffusion of Li ions (Figure S9).

Figure 2d presents the XRD patterns of R-LRM and C-LRM, where all XRD reflections of R-LRM fit well with those of C-LRM, exhibiting a typical hexagonal α -NaFeO₂ layered structure with R-3 m space group and a monoclinic Li_2MnO_3 -like structure with space group C2/m. The weak superlattice diffraction peaks within the range of 20°–25° correspond to the monoclinic Li_2MnO_3 (space group C2/m) component, and the distinct diffraction peaks for the (006)/(102) and (018)/(110) planes indicate a well-structured layered structure. The magnified view of the (003) diffraction peak shows that the diffraction peak of R-LRM has shifted to a lower angle (Figure S10), which can be attributed to the increased interlayer spacing, corresponding to the HRTEM results.^[34,35] Raman spectroscopy is used to characterize the surface phase structure with short-range order (Figure 2e), where the characteristic peaks located at 605 and 488 cm^{-1} correspond to the E_g (O–M–O bending) and A_{1g} (M–O stretching) vibrations in the R-3 m layered structure, and the peaks located at 329, 372, and 434 cm^{-1} indicate the presence of the C2/m space group corresponding to the

Li_2MnO_3 component. This is consistent with the XRD results, indicating that R-LRM has a good crystal structure.^[36]

X-ray photoelectron spectroscopy (XPS) was used to analyze the changes in the valence states of the surface elements, and the binding energy of C 1s (284.80 eV) was used as the reference for peak calibration. The overall spectrum shows that R-LRM contains only Li, Ni, Co, Mn, and O elements, without any impurities such as Al and Cu (Figure S11). As shown in Figure S12, the Co 2p spectrum could be divided into two parts, including Co 2p_{1/2} and Co 2p_{3/2} with their satellite peaks, indicating the coexistence of Co^{3+} and Co^{2+} cations. Due to the similar ionic radius between Ni^{2+} and Li^+ , the presence of a high content of Ni^{2+} can easily enter the Li^+ layer, causing the cationic mixing with low electrochemical properties. From the results of Figure S13, Ni^{3+} takes up $\approx 48.83\%$ of the total Ni element for the C-LRM materials. In contrast, the percentage of Ni^{3+} increases to a higher value of 53.64% for R-LRM, indicating that there is less cationic mixing in regenerated materials due to the unique recycling method based on the double-salt fusion method.^[35,37] Similarly, the Mn 2p spectrum for R-LRM clearly shows two pairs of peaks belonging to Mn^{3+} and Mn^{4+} , with a lower ratio of 25.07% than that of C-LRM (43.13%) (Figure S14). The low proportion of Jahn-Teller active Mn^{3+} reduces the dissolution and irreversible phase transition of Mn, which is beneficial to maintaining structural stability during repeated charge/discharge processes.^[38,39]

Oxygen vacancy is very important in LRM, which can accelerate the migration of TM ions and cause irreversible structural changes, resulting in structural degradation and voltage hysteresis. By actively regulating the oxygen vacancy, the reversibility of anionic redox reaction can be improved, the negative effects caused by anionic redox can be mitigated, and the overall electrochemical performance of the material can be enhanced. Compared with the oxygen vacancy, the stability of lattice oxygen is crucial for maintaining the structural stability of the material, and stable lattice oxygen can enhance the structural stability during the cycle.^[40,41] Here, we further analyzed the content of oxygen vacancy in various materials by electron paramagnetic resonance (EPR) and XPS spectroscopy (Figure 2f and g). The O 1s XPS spectrum exhibits three peaks located at 529.49, 531.51, and 533.68 eV, corresponding to lattice oxygen (TM-O), oxygen vacancies ($\text{C}=\text{O}/\text{CO}_3^{2-}$), and chemisorbed oxygen species. Compared with C-LRM (Figure S15), R-LRM has a higher lattice oxygen content, indicating that it has a more stable lattice oxygen structure. In our cathode regeneration strategy, the double salt-assisted method is used during the co-precipitation process of precursors, which can inhibit the oxidation of lattice oxygen to oxygen vacancy and form more stable lattice oxygen, further promoting the structural stability of regenerated LRM.^[42,43]

2.3. Electrochemical Performance of Regenerated Cathodes

The electrochemical performance of R-LRM and C-LRM was further evaluated by assembling the half cells paired with Li foil as the anode in the voltage range between 2.0 V and 4.8 V. The comparative electrochemical cycling performance at 1.0C (1.0C = 270.00 mAh g⁻¹) shows that the R-LRM cathode still

maintains a specific capacity of 132.67 mAh g⁻¹ after 500 cycles with a high capacity retention rate of 72.45%, while the C-LRM cathode only retains a capacity of 89.59 mAh g⁻¹ with a capacity retention of 49.71% (Figure 3a and Figure S16). At a current density of 0.5C, R-LRM demonstrates an initial discharge capacity of 234.44 mAh g⁻¹, retaining 79.23% of its capacity after 200 cycles (Figure 3b). In comparison, C-LRM shows an initial discharge capacity of 210.45 mAh g⁻¹, with a capacity retention rate of 77.23%. The corresponding charging/discharging curves in Figure S17 exhibit representative charging voltage profiles associated with the Li extraction phenomenon from the rhombohedral LiTMO_2 phase under 4.4 V and the monoclinic Li_2MnO_3 phase over 4.4 V.^[40,44] The improved cycling performance of R-LRM can be attributed to the higher concentration of Mn^{4+} , which can suppress the structural distortion and Jahn-Teller effect, thus improving the cycling stability. In addition, the increase of lattice oxygen content also promotes the improvement of material cycle stability. The rate performance of the R-LRM cathode was experimented at increasing current rates ranging from 0.1 C to 10 C, which delivered a specific discharging capacity of 277.05, 256.92, 226.28, 197.83, 162.30, 118.24, 90.49, and 79.887 mAh g⁻¹, respectively. When abruptly switching the current rate back to 0.1 C, the capacity of the R-LRM cathode recovered to the original level (Figure 3c). As plotted in Figure 3d, the half cells with various active material loadings of 5.48, 8.06, 10.99, and 12.28 mg cm⁻² deliver the reversible area capacities of 1.18, 1.61, 2.24, and 2.49 mAh cm⁻², respectively. The dQ/dV (where Q is capacity and V is voltage) curves in Figure S18 and S19 further illustrate the redox reactions during the charging/discharging processes. There are two redox-active regions, one at ≈ 3.9 V corresponding to the redox reactions of $\text{Ni}^{2+/3+/4+}$ and $\text{Mn}^{3+/4+}$, and one at ≈ 4.5 V corresponding to the oxidation reaction of oxygen. The redox peaks that remain constant in intensity during cycling indicate that Li^+ is reversibly inserted/extracted from the active material. Introducing the double-salt fusion method during regeneration processes can stabilize the lattice oxygen on the surface of R-LRM and reduce the irreversible oxygen loss. Figure S20 shows cyclic voltammetry curves of different cathodes at a scanning rate of 0.1 mV s⁻¹. The oxidation peak near 4.0 V corresponds to the oxidation of $\text{Ni}^{2+}/\text{Co}^{3+}$ to $\text{Ni}^{4+}/\text{Co}^{4+}$, accompanied by the deintercalation of Li^+ from the Li metal anode. The oxidation peak at 4.5 V is a characteristic peak of the electrochemical activation process of the Li_2MnO_3 phase. It is worth noting that the R-LRM cathode exhibits a more obvious plateau, indicating lower polarization and reduced oxygen release compared with the C-LRM.^[36]

Additionally, the diffusion of Li ions in the system can be quantified using the following formula

$$D_{\text{Li}^+} = \left[\frac{i_p \div v^{1/2}}{2.69 \times 10^5 n^{3/2} A C^*} \right] \quad (4)$$

where n is the number of electrons transferred during the redox process, i_p represents peak current, A is the area of the electrode (cm²), D_{Li^+} is the diffusion coefficient of lithium ions (cm² s⁻¹), and C^* is the concentration of lithium ions (mol cm⁻³). Figure 3e and Figure S21 display the cyclic voltammetry (CV) curves of R-LRM and C-LRM at different scan rates, which exhibit a good linear

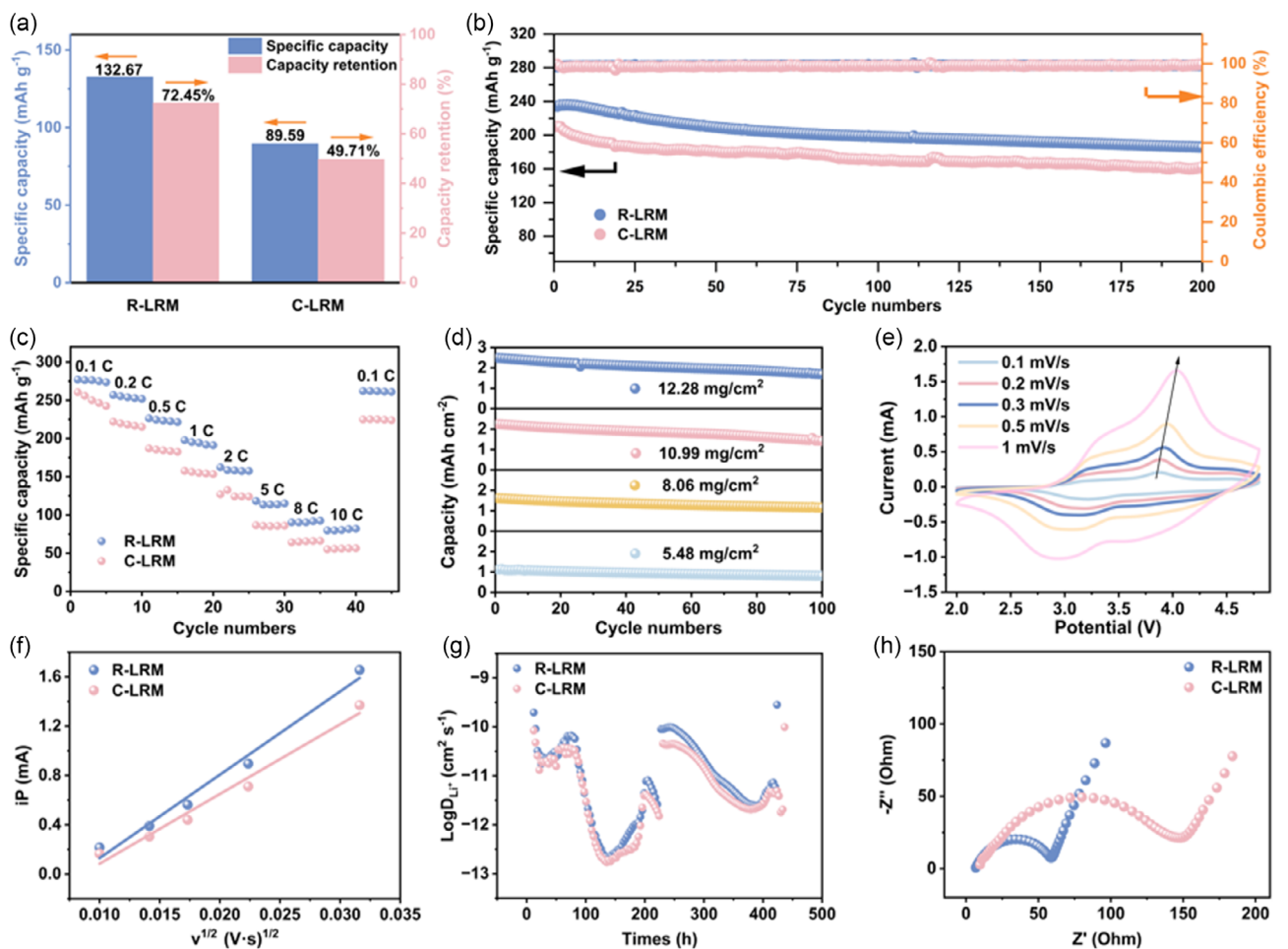


Figure 3. a) Residual capacity and capacity retention of R-LRM and C-LRM after 500 cycles. b) Cycling performance of various cathodes under 0.2C. c) Rate performance of R-LRM and C-LRM. d) Cycling stability of R-LRM under various mass loading. e) CV curves of R-LRM under different scan rates, and f) the corresponding plotted relationship between peak current density and sweep rate. g) GITT and h) EIS curves of various cathodes.

relationship between the square root of the oxidation peak current (i_p) and the scan rate ($v^{1/2}$, Figure 3f). It can be observed that R-LRM exhibits a higher D_{Li^+} coefficient of $cm^2 s^{-1}$, confirming its superior electrochemical performance. In addition, galvanostatic intermittent titration technique (GITT) was used to evaluate the electrochemical reaction kinetics of the material. The GITT curves and the corresponding calculated Li^+ diffusion coefficient D_{Li^+} are shown in Figure 3g. Overall, R-LRM exhibits the highest D_{Li^+} (2.54×10^{-11}), while C-LRM shows the lowest (1.10×10^{-11}). The CV data at different scan rates results are consistent with the GITT findings, indicating that R-LRM possesses higher Li^+ diffusion kinetics. To further verify the earlier results, electrochemical impedance spectroscopy (EIS) was performed (Figure 3h). It was observed that the resistance of the R-LRM cathode was lower than that of the C-LRM cathode, indicating that the R-LRM has better charge transfer kinetics.

2.4. Improved Stability of Regenerated Cathodes

In situ XRD measurement of R-LRM was conducted to further confirm the stability of the crystal structure during cycling (Figure 4a). At a current density of 0.2C between 2.0 and

4.8 V, the deviation of the (003) peak implies crystal structure evolution. During the initial charging process, the (003) diffraction peak shifts to a lower scattering angle corresponding to the Li^+ delithiation, which results in an enhanced Coulombic repulsion between the oxygen layers. The subsequent charging process to 4.8 V exhibits a peak contraction due to the release of lattice oxygen and the Li^+ deinsertion from the TM layer. A completely contrary tendency for the (003) diffraction peak can be observed when transferring to the discharging process.^[38] In the first three cycles, there was no obvious shift in the inner angle and position of the peak, indicating good structural stability of regenerated cathode materials. Focused ion beam/scanning electron microscopy (FIB-SEM) was further used to investigate the structural evolution of various materials, where the C-LRM cathode exhibits obvious cracks and structural collapse after cycles due to structural distortion. Additionally, cracks confined to the near-surface region may result from uneven Li^+ concentration distribution between the particle center and the edges during prolonged cycling. These cracks lead to new surface exposure, intensified interfacial side reactions, and increased polarization, which ultimately have a negative impact on the cycling performance. In sharp contrast, the R-LRM cathode remains a dense

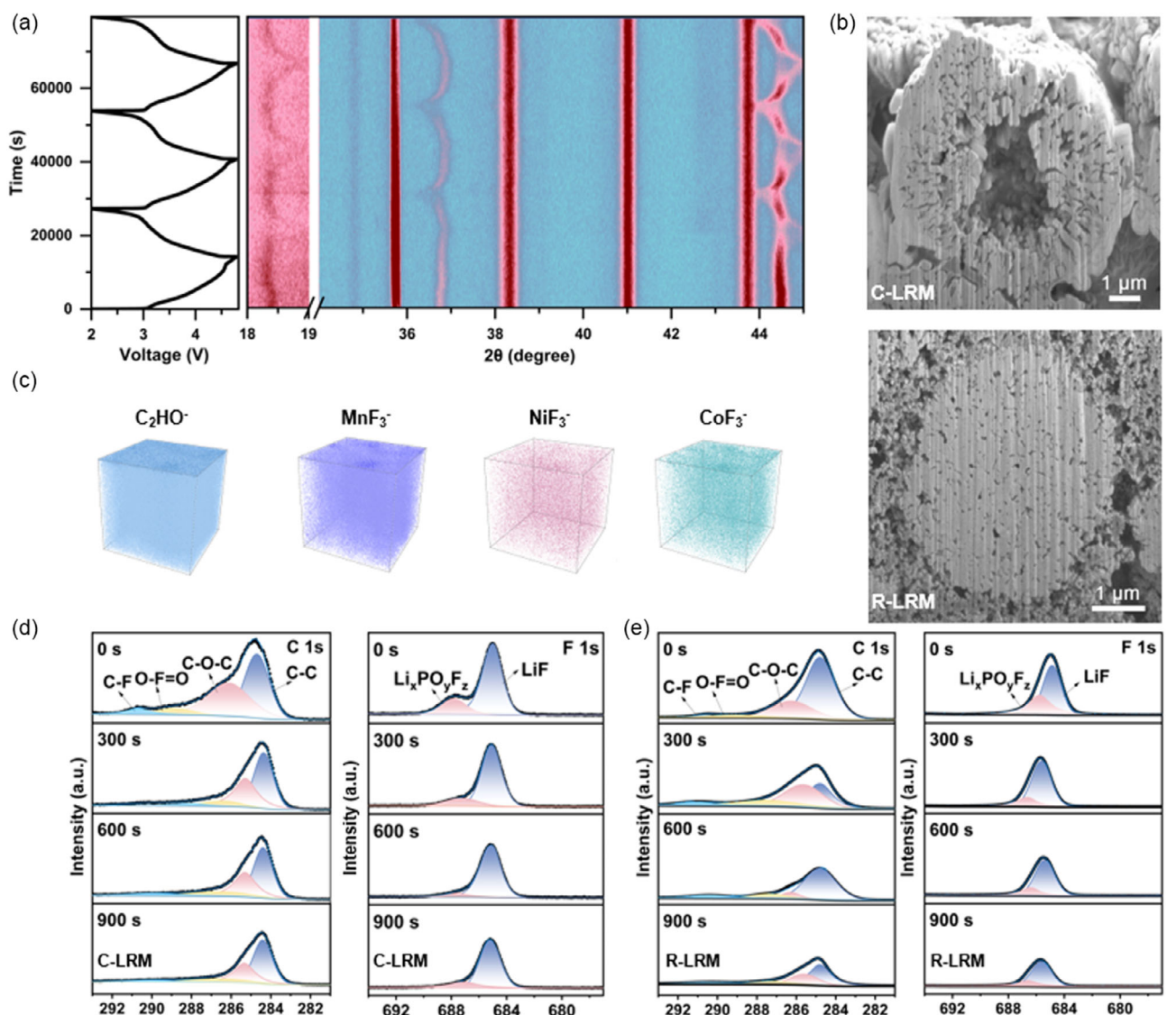


Figure 4. a) In situ XRD results and corresponding cycling curves of the R-LRM. b) FIB-SEM images of C-LRM (up) and R-LRM (down) after cycles. c) TOF-SIMS 3D reconstruction of the representative C_2HO^- , MnF_3^- , NiF_3^- , and CoF_3^- species on the electrode surface. d,e) XPS patterns with a different etching depth of F 1s and C 1s for d) C-LRM and e) R-LRM.

spherical structure without any radial cracks and structural collapse, further confirming the good structural stability of our regenerated materials (Figure 4b).

The oxidative decomposition of the electrolyte will lead to the formation of a cathode electrolyte interphase (CEI) layer on the surface of cathode materials, which consists of various organic and inorganic complexes that can induce negative effects on the cathode materials.^[36,44] An ideal CEI layer should be chemically and electrochemically stable to isolate the cathode from the electrolyte and maintain the structural stability of the cathode materials under harsh operating conditions. Time-of-flight secondary ion mass spectrometry (TOF-SIMS) was employed to investigate the chemical composition and distribution of CEI layers, where the 3D reconstruction TOF-SIMS images show that inorganic signals (NiF_3^- , CoF_3^- , MnF_3^- , and LiF^-) and organic signals (C_2HO^- , F_2^- and PO_2^-) are accumulated on the surface of the cycled R-LRM cathode (Figure 4c and Figure S22). The buildup of organic species and

accumulation of inorganic species at the interface are further confirmed by the corresponding normalized depth profiling in Figure S23. The obtained stable organic-inorganic hybrid CEI layer can reduce side reactions and avoid the dissolution of active substances, which is beneficial to improve Coulombic efficiency and cycle stability. The composition of the CEI layer on the surfaces of R-LRM and C-LRM electrodes after 100 cycles was further characterized by XPS analysis for an in-depth examination (Figure 4d and e). From the C 1s spectrum, the intensities of organic C—O—C and O=C=O species on the surface of R-LRM are lower than those of C-LRM at different etching depths, which indicates a lower content of organic components and carbonate groups for R-LRM due to the formation of a thin CEI layer, further confirming that the decomposition of electrolyte is effectively reduced due to the structural stability of regenerated cathode materials. Furthermore, compared to C-LRM, the R-LRM cathode has relatively lower LiF content on the surface and inner region of the CEI layer in the F 1s spectrum,

Table 1. Comparison of leaching and performance of R-LRM materials.

Black mass	Leaching agent	Product	Extraction efficiency	Wastewater Recycling	Electrochemical Performance	Ref.
NCM111/LMO	Organic Acid (Acetic Acid)	LRM	Li (100.00%), Ni (100.00%), Co (100.00%), Mn (>96.03%)	Yes	277.05 mAh g ⁻¹ at 0.1C	This work
NCM523/LMO	Mineral Acids (HCl)	Co-LNMO	TM>99.9%	No	≈130.0 mAh g ⁻¹ at 1C	[20]
NCM 622	Mineral Acids (H ₂ SO ₄)	NCM622	Li (94.47%), Ni (99.36%), Co (99.28%), Mn (99.56%)	No	192.1 mAh g ⁻¹ at 0.1C	[25]
NCM111/LiCoO ₂ /LMO	Organic Acid (Acetic Acid)	NCM811/111	>99.8%	Yes	161.9 mAh g ⁻¹ at 0.2C	[26]
NCM523	Organic Acid (Citric Acid)	NCM523	Li (99.2%), Ni (99.5%), Co (99.4%), Mn (99.7 %)	Yes	167.6 mAh g ⁻¹ at 0.1C	[46]
NCM622	Organic Acid (H ₂ C ₂ O ₄)	NCM622	Li (92%)	No	179.2 mAh g ⁻¹ at 0.2C	[47]

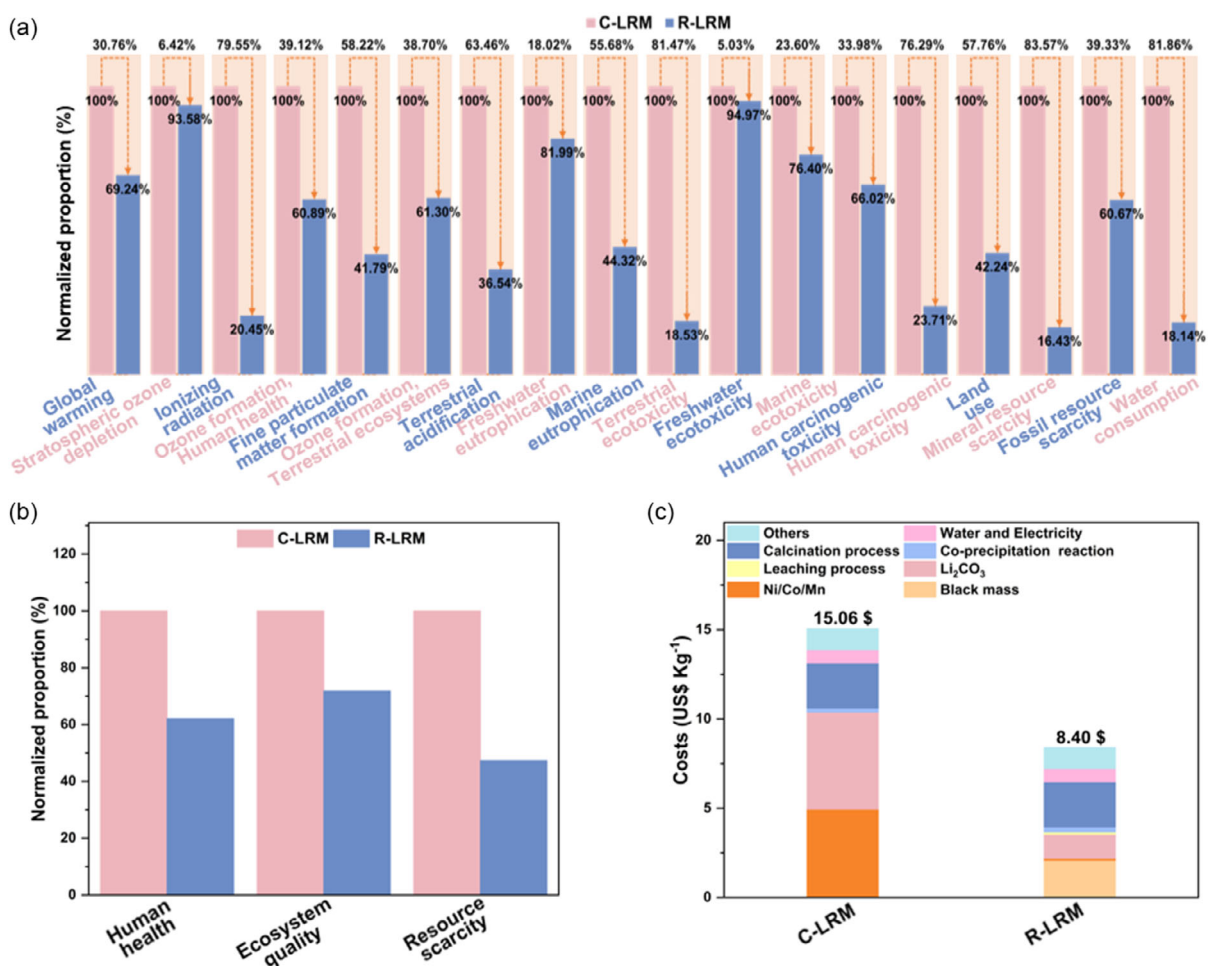


Figure 5. LCA of a) 18 midpoint environmental impact categories after normalization and b) corresponding three endpoint impact categories after normalization. c) Comparison of the costs between commercial cathode manufacturing and our cathode regeneration process.

indicating fewer side reactions at the electrode interface. These results indicate that R-LRM has a more stable interfacial layer and fewer side reactions during long-term cycling.^[39,45]

2.5. Life Cycle and Technoeconomic Analysis

Table 1 summarizes the comparison of various regeneration methods in terms of leaching efficiency, environmental

protection, and sustainability. Our regeneration method utilizes mixed black mass as the raw material, which enhances the efficiency of the crushing and separation processes for upstream spent batteries, thereby facilitating more sustainable and streamlined recycling. Furthermore, our method leverages organic acids, which are significantly more environmentally and human-friendly than conventional mineral acids reported in the literature. This approach not only aligns with the principles of green chemistry

but also achieves the highest leaching rate for high-valent metals, demonstrating superior efficiency and sustainability. The regenerated cathode material exhibits superior performance compared to commercial counterparts, further advancing the closed-loop recycling of spent batteries and enhancing the overall sustainability of the battery life cycle.

In addition, a life cycle assessment (LCA) was conducted based on the production of 1 kg of various cathode powders (Figure S24–S25 and Table S3–S9). First, the 18 midpoint environmental impact categories, including 100-year time-horizon global warming potential, stratospheric ozone depletion, ionizing radiation, ozone formation, human health, fine particulate matter formation, ozone formation, terrestrial ecosystems, terrestrial acidification, freshwater eutrophication, marine eutrophication, terrestrial ecotoxicity, freshwater ecotoxicity, marine ecotoxicity, human carcinogenic toxicity, human noncarcinogenic toxicity, land use, mineral resource scarcity, fossil resource scarcity, and water consumption were considered here, where the regeneration method for R-LRM demonstrated advantages over the production of C-LRM across all 18 midpoint environmental impact categories after normalization (Figure 5a). A substantial reduction of environmental impact in these 18 midpoint categories between 6.42% and 83.57% can be observed due to our advanced cathode regeneration strategy and improved recycling equipment systems. As shown in Figure 5b, these 18 midpoint environmental impact categories are condensed into 3 endpoint impact categories, including human health, ecosystem quality, and resource scarcity. The comprehensive comparison of the three key aspects provides a clearer illustration of the benefits of R-LRM production for human health (62.11%), ecosystem quality (71.78%), and resource scarcity (47.30%) compared to the commercial manufacturing of C-LRM after normalization. These LCA results highlight that these regeneration methods offer environmentally beneficial solutions for managing spent LIBs, emphasizing their potential to reduce environmental impact while facilitating the transition to next-generation high-energy-density LIBs.

The techno-economic analysis of regenerated cathode materials in the battery recycling process is a critical factor that has captured the interest of researchers and recycling companies. By showcasing both economic viability and environmental advantages, such evaluations can foster increased investment and drive innovation in sustainable cathode regeneration technologies. The manufacturing cost of 1 kg of C-LRM is ≈US\$15.06, while the cost of producing 1 kg of R-LRM is only US\$8.40, a decrease of ≈44.22% (Figure 5c). The decisive factors for the cost of C-LRM and R-LRM are the price of raw materials, Li_2CO_3 , and the high-temperature calcination process. As for equipment, the customized CSTR system we designed is almost identical to the commercial reactor and does not require major modifications. This also greatly reduces the additional equipment cost in the recycling process, resulting in the same equipment cost as manufacturing commercial cathode materials. These results indicate that, in addition to electrochemical performance, our cathode regeneration process also offers significant advantages in terms of cost and ecological impact, demonstrating its strong competitiveness and its role in facilitating the transition from spent Li-ion batteries to more sustainable next-generation battery systems.

3. Conclusion

In summary, a scalable and efficient cathode regeneration method is proposed to reconstruct LRM with improved structural stability and electrochemical performance for the next-generation high-energy-density LIBs. With the help of our customized commercial-grade CSTR system, a high recycling efficiency of over 97.38% is achieved for the selective high-value TM elements, and the output of each reaction is about 5.40 kg. Specifically, higher capacity retention over 500 cycles with a specific capacity of 277.05 mAh g⁻¹ is achieved, which is 14.26% and 22.74% better than commercial state-of-the-art cathode materials. While reducing costs by 44.22%, our cathode regeneration strategy has significant optimization advantages in resource scarcity, human health, and ecosystem quality impacts. This study highlights the significant potential of cathode regeneration strategies in mitigating the environmental impact of spent LIBs and reducing the reliance on rare elements in current cathode production, thereby paving the way for the sustainable development of the next-generation sustainable LIB industry.

4. Experimental Section

Materials Synthesis

All chemical reagents (Analytical Reagent grade, AR) were purchased from Shanghai Aladdin Biochemical Technology Co., Ltd., except where noted: acetic acid (\geq 99.8%), hydrogen peroxide (30% w/w), Li_2CO_3 (\geq 99%), $\text{NH}_3\text{H}_2\text{O}$ (GR, 25%–28%), NaHCO_3 (\geq 99.8%), NaCl (\geq 99.5%), and KCl (\geq 99.0%). In the experiment, a set of customized CSTR systems was used to extract high-value elements from the black mass and prepare the cathode precursors. The spent NCM and LiMn_2O_4 powder were added to a solution of 3.0 M acetic acid and 2.0 vol% hydrogen peroxide, and the mixture was leached at 70 °C under nitrogen protection for 2 h.

To obtain the R-LMO cathode material, the molar ratio of Ni, Co, and Mn in the black mass leachate was adjusted to \approx 0.54:0.13:0.13 by adding LiMn_2O_4 -based leachate. After that, all the transition metal ions in the solution were coprecipitated using 1.0 M NaHCO_3 (aq.) solution, which was pumped into the continuously stirred reactor (molar ratio of HCO_3^- /transition metals = 1.5: 1). At the same time, 2.0 M $\text{NH}_3\text{H}_2\text{O}$ (aq.) was used to adjust the pH of the solution. The temperature of the reactor was controlled at 70 °C, and the pH value of the system was controlled at pH = 8.2. After filtration and washing with deionized water, lithium carbonate (Li_2CO_3) and precursor powder were evenly mixed by a ball mill at the molar ratio of 1.25:1.00, followed by high-temperature calcination. During the calcination process, the double salt fusion method was implemented, incorporating NaCl (three times the precursor's mass) and KCl (twice the precursor's mass) for roasting. The temperature was raised to 850 °C at a rate of 5 °C min⁻¹ and sustained for 12 h.

Materials Characterization

The crystal structure of the samples was analyzed using Cu K α XRD (Empyrean S3). The morphology of the samples was characterized with SEM (Sigma 560). Transmission electron microscopy (TEM, JEM 2100 F) was employed to observe the morphology and lattice fringes. XPS data were obtained using a Thermo Fisher Escalab 250 Xi+ spectrometer. The concentration of metal ions in the leachate and regenerated materials was determined using ICP-OES (Avio 550 Max).

Electrochemical Measurements

The mixture of active materials (70 wt%), Super P (20 wt%), and polyvinylidene fluoride (10 wt%) was coated onto aluminum foil with the help of N-methyl pyrrolidone solution and dried at 60 °C for 12 h. The electrodes were assembled into CR2032 coin cells with lithium metal as the counter electrode, Celgard 2400 as the separator, and electrolyte (111 high-voltage electrolyte, dodochem). The coin cells were assembled and disassembled in an inert atmosphere inside an argon-filled glove box. The constant current charging–discharging performance and cyclic voltammetry in the voltage range of 2.0–4.8 V were tested using the Neware battery testing system and CHI660E (Shanghai Chenhua Instrument Co., Ltd.). EIS measurements were conducted in the frequency range of 0.01 to 105 Hz, with an amplitude of 5 mV.

Life Cycle Assessment

Environmental impacts of the production of C-LRM and R-LRM were analyzed using the LCA approach, followed by the International Organization for Standardization standards 14 040 and 14 044 series. The corresponding environmental impacts were simulated using SimaproTM 9.4.0.1 software with the Ecoinvent (v3.8) databases as inventories. The production of 1.0 kg cathode material was considered as the functional units. The environmental impact equivalent of recycled spent cathode materials compared to commercial materials was based on the economic allocation. The ReCiPe 2016 Midpoint (H) V1.07/World (2010) H method and IPCC 2021 GWP100 V1.01 method with units and abbreviations were used for the calculation of 18 midpoint environmental impact categories, which were further aggregated into three endpoint impact categories (human health, ecosystem quality, and resource scarcity) based on ReCiPe 2016 Endpoint (H) V1.07/World (2010) H/ A method.

Acknowledgements

H.Q. and X.S. contributed equally to this work. This work was supported by the financial support from the Strategic Priority Research Program of the Chinese Academy of Sciences (XDB0600400), the Program for Jiangsu Specially-Appointed Professors, the Science and Technology Major Project of Liaoning Province (2024JH1/11700013), the Natural Science Foundation of Hebei Province, China (B2021202028), and the Program for the Outstanding Young Talents of Hebei Province, China.

Conflict of Interest

The authors declare no conflict of interest.

Data Availability Statement

The data that support the findings of this study are available from the corresponding author upon reasonable request.

Keywords: cathode regeneration · life cycle assessments · lithium-rich manganese-based cathodes · spent lithium-ion batteries · sustainability

- [1] L. Men, S. Feng, J. Zhang, X. Luo, Y. Zhou, *Green Chem.* **2024**, *26*, 1170.
- [2] B. K. Biswal, B. Zhang, P. T. M. Tran, J. Zhang, R. Balasubramanian, *Chem. Soc. Rev.* **2024**, *53*, 5552.
- [3] T. Yang, D. Luo, A. Yu, Z. Chen, *Adv. Mater.* **2023**, *35*, 2203218.
- [4] J. Wang, Y. Lyu, R. Zeng, S. Zhang, K. Davey, J. Mao, Z. Guo, *Energy Environ. Sci.* **2024**, *17*, 867.
- [5] K. Vinayak Anil, Z. Xu, G. Li, X. Wang, *Renewables* **2023**, *1*, 294.
- [6] J. Mao, C. Ye, S. Zhang, F. Xie, R. Zeng, K. Davey, Z. Guo, S. Qiao, *Energy Environ. Sci.* **2022**, *15*, 2732.
- [7] E. Fan, J. Lin, X. Zhang, R. Chen, F. Wu, L. Li, *Small Methods* **2021**, *5*, 2100672.
- [8] Y. Lan, X. Li, G. Zhou, W. Yao, H.-M. Cheng, Y. Tang, *Adv. Sci.* **2024**, *11*, 2304425.
- [9] X. Liu, R. Wang, S. Liu, J. Pu, H. Xie, M. Wu, D. Liu, Y. Li, J. Liu, *Adv. Energy Mater.* **2023**, *13*, 2302987.
- [10] J. Shuai, W. Liu, S. Rohani, Z. Wang, M. He, C. Ding, X. Lv, *Chem. Eng. J.* **2025**, *503*, 158114.
- [11] N. Ogihara, K. Nagaya, H. Yamaguchi, Y. Kondo, Y. Yamada, T. Horiba, T. Baba, N. Ohba, S. Komagata, Y. Aoki, H. Kondo, T. Sasaki, S. Okayama, *Joule* **2024**, *8*, 1364.
- [12] Y. Han, M. Yan, Y. Fang, Y. Xiong, Y. Wang, Y. Chen, L. Lin, J. Qian, T. Mei, X. Wang, *J. Power Sources* **2024**, *603*, 234417.
- [13] H. Zhou, Y. Zhang, L. Li, Z. Cao, *Green Chem.* **2023**, *25*, 7696.
- [14] P. K. Choubey, O. S. Dinkar, R. Panda, A. Kumari, M. K. Jha, D. D. Pathak, *Waste Manage.* **2021**, *121*, 452.
- [15] H. Li, Y. Chen, Z. Cui, Y. Su, Z. Liu, X. Dong, Z. L. Wang, W. Tang, *J. Hazard. Mater.* **2025**, *484*, 136769.
- [16] J. Lin, C. Cui, X. Zhang, E. Fan, R. Chen, F. Wu, L. Li, *J. Hazard. Mater.* **2022**, *424*, 127757.
- [17] M. A. Hasan, R. Hossain, V. Sahajwalla, *Green Chem.* **2025**, *27*, 1073.
- [18] X. Qu, B. Zhang, J. Zhao, B. Qiu, X. Chen, F. Zhou, X. Li, S. Gao, D. Wang, H. Yin, *Green Chem.* **2023**, *25*, 2992.
- [19] Z. Fei, Y. Su, Y. Zha, X. Zhao, Q. Meng, P. Dong, Y. Zhang, *Chem. Eng. J.* **2023**, *464*, 142534.
- [20] J. Ma, J. Wang, K. Jia, Z. Liang, G. Ji, H. Ji, Y. Zhu, W. Chen, H. Cheng, G. Zhou, *Nat. Commun.* **2024**, *15*, 1046.
- [21] H. Ji, J. Wang, H. Qu, J. Li, W. Ji, X. Qiu, Y. Zhu, H. Ren, R. Shi, G. Ji, W. Zhao, G. Zhou, *Adv. Mater.* **2024**, *36*, 2407029.
- [22] J. Wang, J. Ma, Z. Zhuang, Z. Liang, K. Jia, G. Ji, G. Zhou, H.-M. Cheng, *Chem. Rev.* **2024**, *124*, 2839.
- [23] Z. Qin, T. Zhang, X. Gao, W. Luo, J. Han, B. Lu, J. Zhou, G. Chen, *Adv. Mater.* **2024**, *36*, 2307091.
- [24] H. Yu, H. Yang, K. Chen, L. Yang, M. Huang, Z. Wang, H. Lv, C. Xu, L. Chen, X. Luo, *Energy Storage Mater.* **2024**, *67*, 103288.
- [25] Y. Sun, H. Yang, J. Li, X. Zhuge, Y. Ren, Z. Ding, *J. Power Sources* **2024**, *602*, 234407.
- [26] T. Yang, D. Luo, X. Zhang, S. Gao, R. Gao, Q. Ma, H. W. Park, T. Or, Y. Zhang, Z. Chen, *Nat. Sustain.* **2024**, *7*, 776.
- [27] X. Ji, Q. Xia, Y. Xu, H. Feng, P. Wang, Q. Tan, *J. Power Sources* **2021**, *487*, 229362.
- [28] S. Zhao, K. Yan, J. Zhang, B. Sun, G. Wang, *Angew. Chem. Int. Ed.* **2021**, *60*, 2208.
- [29] Q. Huang, J. Liu, X. Chen, P. Zhang, L. Lu, D. Ren, M. Ouyang, X. Liu, *Adv. Mater.* **2025**, *37*, 2410006.
- [30] M. Kaya, *Circular Economy* **2022**, *1*, 100015.
- [31] Z. Zheng, D. Xie, X. Liu, H. Huang, M. Zhang, F. Cheng, *ACS Appl. Mater. Interfaces* **2024**, *16*, 31137.
- [32] A. Zorin, T. Song, D. Gastol, E. Kendrick, *Metals* **2023**, *13*, 1276.
- [33] W. Gao, J. Song, H. Cao, X. Lin, X. Zhang, X. Zheng, Y. Zhang, Z. Sun, *J. Cleaner Prod.* **2018**, *178*, 833.
- [34] Y. A. Li, Q. Wang, K. Niu, X. Li, X. Dai, Y. Yin, G. Huang, B. Xing, C. Zhang, Z. Chen, *J. Power Sources* **2024**, *613*, 234844.
- [35] Z. Li, C. Guo, S. Cao, H. Li, J. Chen, L. Wu, R. Wang, Y. Bai, X. Wang, *J. Alloys Compd.* **2024**, *984*, 173954.
- [36] X. Sun, C. Qin, B. Zhao, S. Jia, Z. Wang, T. Yang, X. Liu, L. Pan, L. Zheng, D. Luo, Y. Zhang, *Energy Storage Mater.* **2024**, *70*, 103559.
- [37] W. Fu, T. Lei, B. Cao, X. Shi, Q. Zhang, Z. Ding, L. Chen, J. Wu, *J. Power Sources* **2024**, *618*, 235144.
- [38] L. Wang, L. Xu, W. Xue, Q. Fang, H. Liu, Y. Liu, K. Zhou, Y. Li, X. Wang, X. Wang, X. Yang, X. Yu, X. Wang, *Nano Energy* **2024**, *121*, 109241.
- [39] J. Liu, T. Dong, X. Yuan, Y. Cui, Y. Liu, C. Chen, H. Ma, C. Su, H. Zhang, S. Zhang, *Adv. Energy Mater.* **2023**, *13*, 2300680.
- [40] X. Liu, J. Cheng, Y. Guan, S. Huang, F. Lian, *Mater. Chem. Front.* **2023**, *7*, 3434.
- [41] Z. Li, S. Cao, C. Wu, H. Li, J. Chen, W. Guo, B. Chang, Y. Shen, Y. Bai, X. Wang, *J. Power Sources* **2022**, *536*, 231456.
- [42] W. Yu, L. Zhao, Y. Wang, C. Yang, J. Wang, H. Huang, A. Wu, X. Dong, G. Cao, *J. Colloid Interface Sci.* **2023**, *648*, 820.

- [43] S. Kang, X. Wei, Y. Chu, Y. Mu, L. Zou, X. Xu, Q. Zhang, L. Zeng, *J. Mater. Chem. A* **2024**, *12*, 9584.
- [44] Y. Yang, C. Gao, T. Luo, J. Song, T. Yang, H. Wang, K. Zhang, Y. Zuo, W. Xiao, Z. Jiang, T. Chen, D. Xia, *Adv. Mater.* **2023**, *35*, 2307138.
- [45] W. Guo, Y. Zhang, L. Lin, Y. Liu, M. Fan, G. Gao, S. Wang, B. Sa, J. Lin, Q. Luo, B. Qu, L. Wang, J. Shi, Q. Xie, D.-L. Peng, *Small* **2023**, *19*, 2300175.
- [46] M. Zhou, J. Shen, Y. Duan, Y. Zuo, Z. Xing, R. Liu, *Energy Storage Mater.* **2024**, *67*, 103250.
- [47] Z. Huang, X. Liu, Y. Zheng, Q. Wang, J. Liu, S. Xu, *Chem. Eng. J.* **2023**, *451*, 139039.

Manuscript received: April 27, 2025

Revised manuscript received: June 21, 2025

Version of record online:
